Multiscale modeling of Schottky-barrier MOSFETs with disilicide source/drain contacts: Role of contacts in the carrier injection

M. Dubois,[1,*] D. Jiménez,[2] P. L. de Andres,[3] and S. Roche[1]
[1]*CEA-DRFMC/SPSMS/GT, 17 rue des Martyrs, 38054 Grenoble Cedex 09, France*
[2]*Departament d'Enginyeria Electrònica, Escola Tècnica Superior d'Enginyeria, Universitat Autònoma de Barcelona, 08193 Bellaterra, Spain*
[3]*Instituto de Ciencia de Materiales (CSIC), Cantoblanco, E-28049 Madrid, Spain*
(Received 12 March 2007; revised manuscript received 21 May 2007; published 28 September 2007)

We report on a multiscale approach for the simulation of electrical characteristics of metal disilicide based Schottky-barrier metal oxide semiconductor field-effect transistors (SB-MOSFETs). Atomistic tight-binding method and nonequilibrium Green's function formalism are combined to calculate the propagation of charge carriers in the metal and the charge distribution at the $M\mathrm{Si}_2(111)/\mathrm{Si}(111)$ and $M\mathrm{Si}_2(111)/\mathrm{Si}(100)$ (with M =Ni, Co, and Fe) contacts. Quantum transmission coefficients at the interfaces are then computed accounting for energy and momentum conservation, and are further used as input parameters for a compact model of SB-MOSFET current-voltage simulations. In the quest for nanodevice performance optimization, this approach allows unveiling the role of different materials in configurations relevant for heterostructure nanowires.

DOI: 10.1103/PhysRevB.76.115337 PACS number(s): 73.40.−c, 85.35.−p, 73.63.−b, 73.30.+y

I. INTRODUCTION

Scaling down metal oxide semiconductor field-effect transistors (MOSFETs) is one of the most challenging tasks for nanoelectronics device designers. As the physical limits of conventional MOSFETs are being reached, alternative structures are proposed to circumvent or limit parasitic effects that emerge with size reduction, such as increasingly large contact resistances owing to intrusive dopant redistribution at the contact/channel interfaces. Among these candidates, Schottky-barrier MOSFETs (SB-MOSFETs) have been widely investigated in recent years, both experimentally[1] and theoretically.[2–4] In SB-MOSFETs, the highly doped source and drain contacts are replaced by metallic ones, which could reduce, in principle, both contact resistances and short channel effects.[5,6] However, in contrast with the Ohmic contact generally achieved with traditional MOSFETs, SB-MOSFET current-voltage characteristics become largely dominated by the interface electrostatics due to Fermi level pinning.[7] In the past, this phenomenon has been a major drawback to engineering performant, versatile and well controlled transistor devices and logic circuits.[8,9]

Despite this situation, remarkable improvements have been achieved in the past years in the epitaxial growth of high quality NiSi_2 and CoSi_2 films on both (100)- and (111)-oriented silicon substrates, owing to the very similar crystal structures of disilicides and silicon materials.[10] More recently, a metallic phase has been identified for iron disilicide (γ-FeSi_2) with the same fluorite structure although its growth on silicon substrates remains delicate.[11,12] The low Schottky-barrier height (SBH) arising at the interface between these three disilicides and silicon[13,14] makes them promising materials for the fabrication of metal disilicide source/drain SB-MOSFETs with good performances.

Moreover, catalytically grown undoped silicon nanowires (Si-NWs) have been recently made with a further self-aligned formation of nickel silicide (NiSi_x) source and drain segments along the nanowire.[15,16] The initial characterization of these nanodevices shows promising performances, such as large sustained current densities.[16] This opens novel perspectives for large scale integration of low-dimensional SB-MOSFETs using chemically driven bottom-up integration methods.

Finally, first principles calculations[17] suggest that weak doping of the silicon channel could strongly reduce the SBH, bringing silicide/silicon contact resistance way below the targeted value of the International Technology Roadmap for Semiconductors.

Schottky contact resistances between disilicides and silicon-based materials are known, however, to be sensitive to quantum reflection phenomena. These backscattering effects occur during charge transfer at the interface because symmetry-induced selection rules of contacted materials restrict the possibilities to simultaneously conserve energy and momentum.[18] It is, thus, of relevance to explore in depth the material-dependent role played by quantum reflections in order to assess the conditions for the ultimate performances of SB-MOSFETs.

In this work, we present a multiscale modeling of SB-MOSFETs with metal disilicide source and drain contacts, combining atomistic based transport calculations with compact modeling of SB-MOSFET devices. The paper is divided as follows. In Sec. II, the atomistic tight-binding Green's function formalism is detailed, and the ballistic propagation of electrons in the metallic source/drain is computed in Sec. III, taking into account the materials' nature, electronic structure, and symmetry orientations. Quantum reflection phenomena are then addressed in Sec. IV by matching the energy and $\mathbf{k}_\parallel$ vector between outgoing states from the metal and the incoming states in the silicon channel, which is tackled within the effective mass approximation. This allows extracting a transmission coefficient that will be further incorporated into a compact model for the simulation of transistor current-voltage characteristics in a heterostructure nanowire configuration. The theoretical background for this compact model is presented in Sec. V. In this way, we can include

 ©2007 The American Physical Society

complex quantum effects in the study of the material optimization versus the device performances. Results for the device characteristics are presented and discussed in Sec. VI.

II. THEORY OF BALLISTIC TRANSPORT IN THE METAL DISILICIDE CONTACTS

The calculation of the charge transport in the disilicide metal is based on a tight-binding Green's function formalism successfully applied to analyze electronic transport in ballistic electron emission microscopy (BEEM).[19,20] In BEEM experiments, a slice of metal is deposited on a semiconducting substrate. The tip of a scanning tunneling microscope (STM) is used as a microscopic electron gun to inject electrons to the metal, which propagate through the metal, overcome the Schottky barrier at the metal-semiconductor interface, propagate through the n- or p-doped semiconductor, and finally, the current is measured out from a back contact in the semiconductor.

The theoretical model uses a Hamiltonian written in a linear combination of atomic orbitals (LCAOs) basis:

$$H = H_T + H_S + V_{TS}, \tag{1}$$

where H_T defines the tip, H_S the metal sample, and V_{TS} the coupling between the tip and the surface in terms of a hopping matrix, $T_{\alpha m}$, between orbitals in the tip (α) and the surface (m). Propagation of carriers, one of the central key physical processes for modeling MOSFET devices at the atomic level, can be treated very accurately by applying nonequilibrium Keldysh Green's functions.[21,22] In particular, given a Hamiltonian formally separated as two independent terms plus its interaction [Eq. (1)], this formalism allows us to find solutions for the whole system in terms of simpler solutions for each of the two independent parts, and the appropriate Green's functions. From the point of view of transport calculations, this is a truly microscopic formalism, free of adjustable parameters once the Hamiltonians are given in some representation. In order to keep the computational cost of our calculations under control, and keeping in mind that our goal is to compute the corresponding Green's functions, we choose to represent the Hamiltonians for the independent parts of the system in a LCAO basis. Therefore, we can immediately benefit from highly accurate parametrized versions of these Hamiltonians, constructed to coincide along the important symmetry lines of the Brillouin zone with *ab initio* calculations to accuracies better than 1/100, at the inexpensive cost of diagonalizing matrices of quite modest sizes.[28]

The so-called advanced (G^A) and retarded (G^R) Green's functions of the system are defined as

$$G^A(E) = [E - H - i\eta]^{-1},$$
$$G^R(E) = [E - H + i\eta]^{-1}, \tag{2}$$

where an arbitrary small imaginary part η is added to the energy E to ensure convergence. As soon as a bias voltage is applied, the system should be treated as out of equilibrium. It is then convenient to use the Keldysh technique,[21] which corresponds to the generalization of the many-body Green's function theory to systems that are out of equilibrium. Within this formalism, the current between two sites i and j in the sample can be written as

$$J_{ij} = \frac{e}{\pi\hbar}\int \mathrm{Tr}\{T_{ij}(G_{ji}^{+-} - G_{ij}^{+-})\}dE. \tag{3}$$

Matrices G_{ji}^{+-} are nonequilibrium Keldysh Green's functions that for this kind of transport problem can be calculated in terms of the retarded and advanced Green's functions of the interacting system as follows:[22,23]

$$G_{ji}^{+-}(E) = [I + G^R(E)T]g^{+-}[I + TG^A(E)]. \tag{4}$$

In turn, the Green's operators for the interacting system, $G^{R,A}(E)$, can be obtained from the Green's functions of the decoupled systems ($g^{R,A}$) and the operator giving the interaction between them (T) by solving a Dyson-like equation:

$$G^{R,A}(E) = g^{R,A} + g^{R,A}TG^{R,A}. \tag{5}$$

This latter equation, carried out up to infinite order, yields a self-consistent solution for the Green's function of the interacting system in terms of the simpler objects g and T. For our purposes, however, it is enough to take into account that T is not too strong and seek solutions up to second order only. As given in Ref. 20, this reduces our equations to

$$G_{ij}^{+-} = g_{ij} + G_{j0}^R T_{01} g_{1i} + g_{j1} T_{10} G_{0i}^A + G_{j1}^R T_{10} g_{00} T_{01} G_{1i}^A,$$

$$G_{ji}^{+-} = g_{ji} + G_{i0}^R T_{01} g_{1j} + g_{i1} T_{10} G_{0j}^A + G_{i1}^R T_{10} g_{00} T_{01} G_{1j}^A,$$

where the different Keldysh Green's functions (g) are obtained from the equilibrium functions ($g^{R,A}$) and the Fermi distribution functions of the tip (f_T) and the sample (f_S):

$$g_{1i} = f_s(g_{1i}^A - g_{1i}^R),$$

$$g_{j1} = f_s(g_{j1}^A - g_{j1}^R),$$

$$g_{1j} = f_s(g_{1j}^A - g_{1j}^R),$$

$$g_{i1} = f_s(g_{i1}^A - g_{i1}^R),$$

$$g_{00} = 2\pi\rho_{00} f_T,$$

ρ_{00} being the density of states matrix at the 0 site. In these equations, the injection takes place in the 0 site (in the tip), and the hopping matrix T connects this site with the first 1 site in our system.

Plugging these Green's functions in Eq. (3), after some algebra, the current between two sites i and j in the metal can be calculated using the following formula:[20]

$$J_{ij}(V) = \frac{4e}{\hbar}\Im\int_{E_F}^{\mathrm{eV}} \mathrm{Tr}\sum_{m\alpha\beta n}[T_{ij}g_{jm}^R T_{m\alpha}\rho_{\alpha\beta}T_{\beta n}g_{ni}^A]dE, \tag{6}$$

where Greek letters refer to the injecting tip sites and Latin letters to sites inside the sample. $g^{R(A)}$ are the Green's function of the uncoupled parts of the system, and $T_{m\alpha}$ the hopping matrix elements. The integration is performed between

the Fermi level of the metal (E_F) and the applied bias (eV). The symbol $\Im$ stands for the imaginary part of the integral. The summation runs over tunneling active atoms in the injecting tip (α,β) and the sample (m,n). $\rho_{\alpha\beta}$ is the matrix of density of states for the tip: $(g^A_{\alpha\beta}-g^R_{\alpha\beta})=2\pi i\rho_{\alpha\beta}$. The trace denotes summation over the atomic orbitals of the LCAO basis.

To take into account quantum reflection effects inside this microscopic approach to transport, i.e., looking for energy and $\mathbf{k}_\parallel$-vector conservation at the interface, it is necessary to compute the current distribution in reciprocal space. Therefore, the current distribution is expressed between two planes i and j as[19]

$$J_{ij}(\mathbf{k}_\parallel,V)=\frac{4e}{\hbar}\Im\int_{E_F}^{\mathrm{eV}}\mathrm{Tr}\sum_{m\alpha\beta n}[T_{ij}(\mathbf{k}_\parallel)g^R_{jm}(\mathbf{k}_\parallel)T_{m\alpha}(\mathbf{k}_\parallel)\times\rho_{\alpha\beta}(\mathbf{k}_\parallel)T_{\beta n}(\mathbf{k}_\parallel)g^A_{ni}(\mathbf{k}_\parallel)]dE. \tag{7}$$

We notice that all quantities in this equation are the $\mathbf{k}_\parallel$-Fourier transforms of the corresponding objects in Eq. (4).

This theory of BEEM was originally developed to investigate the transport of electrons injected from a STM tip to unoccupied metallic states, i.e., at energies greater than the Fermi level of the metal. In this work, the formulation of the electron distribution has been modified to fit the case where the metal disilicide is actually the reservoir of electrons for the injection in the semiconducting channel of a MOSFET. The main issue was that electrons injected to the channel correspond to electronic states mainly located below the Fermi level, although at room temperature the occupation of levels above E_F is nonzero due to the Fermi-Dirac distribution function. Thus, the position of the metal Fermi level has been artificially modified so that the contribution of electronic states, the energy of which is lower than the true E_F, can be treated. Finally, the simulations will be performed for nanowires with rather large diameter (20 nm). For that reason, the atomistic electrons' transport and current distribution will be calculated for semi-infinite materials, as first intended in the BEEM theory. Yet, this approximation will allow us to use an out-of-equilibrium formalism at an atomistic level of sophistication with a very good level of accuracy.

III. CURRENT DISTRIBUTIONS IN THE METAL DISILICIDE

Calculations using the above formalism have been performed for three different metal disilicides: $NiSi_2$, $CoSi_2$, and γ-$FeSi_2$. All of these crystallize in the fluorite structure (CaF_2), which can be described as two sublattices where the metal atoms (M, in Fig. 1) occupy fcc-like positions, with respective lattice parameters of 5.406,[24] 5.365,[24] and 5.387 Å.[25] The low lattice mismatch with the silicon crystal (0.46%, 1.2%, and 0.82%, respectively) makes possible the growth of these disilicides on both (100)- and (111)-oriented silicon substrates with high quality.[26,27]

The exact electronic structure of each disilicide is calculated using the tight-binding parameters of Ref. 28. The orientation of the metal is chosen so that the interface with

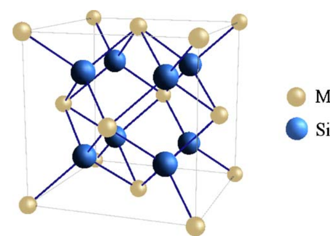

FIG. 1. (Color online) Conventional cell of the fluorite (CaF_2) structure of $NiSi_2$, $CoSi_2$, and γ-$FeSi_2$. Silicon atoms are represented in blue (dark gray) and metal atoms (Ni, Co, or Fe) in beige (light gray).

silicon is made along its (111) surface. The transport calculation is made in the direction perpendicular to that plane. Using the formalism described above, the current distributions are computed in reciprocal space after propagation in 30 layers of metal, which corresponds to a thickness of about 170 Å, large enough to avoid any modification of the charge distribution due to a longer propagation. The 30th layer of metal will, thus, be considered as the interfacial layer with the silicon channel. Finally, the density of disilicide electronic states involved in the transmission would depend on the polarization conditions for the device simulation, meaning the source-drain and gate voltages. The charge distribution at the interface will then be calculated for an energy range wide enough to include all desired conditions applied to the device. Hence, the simulations have been performed for an energy window of $[E_F-0.45\text{ eV}; E_F+1.0\text{ eV}]$.

The evolution of the charge distributions with respect to the energy is presented in Fig. 2 for the three disilicides. In this figure, the current distributions have been plotted in reciprocal space for three different energies corresponding to $E_F-0.3$ eV [Figs. 2(a), 2(d), and 2(g)], $E_F+0.3$ eV [Figs. 2(b), 2(e), and 2(h)], and $E_F+0.7$ eV [Figs. 2(c), 2(f), and 2(i)]. Each dot on the figure is a $\mathbf{k}_\parallel$ vector of the first Brillouin zone (BZ) of the (111)-oriented metal surface. A gray scale is used to represent the density of current associated with each $\mathbf{k}_\parallel$ vector. Figure 2 shows that not only the current distribution strongly depends on the energy but also that the nature of the metal disilicide is very influent. These results demonstrate that considering the exact electronic structure of each material is of crucial importance on the transport properties and, consequently, on the transmission. Although the current distribution in reciprocal space exhibits a threefold symmetry for the three disilicides, the focusing of the charges around the Γ point in the Brillouin zone is different from one material to the other. Hence, $NiSi_2$ shows a stronger localization of the charges around Γ compared to $CoSi_2$ and γ-$FeSi_2$. Moreover, γ-$FeSi_2$ exhibits a lack of charges around this point for high energies [Figs. 2(h) and 2(i)]. This already suggests that the transmission of electrons to the silicon channel will strongly depend on both the injection's energy and the nature of the metal disilicide. Knowing the charges' distribution at the interface, in the reciprocal space, will then allow studying the conservation laws for energy and momentum that play the key role for the transmission in the silicon channel.

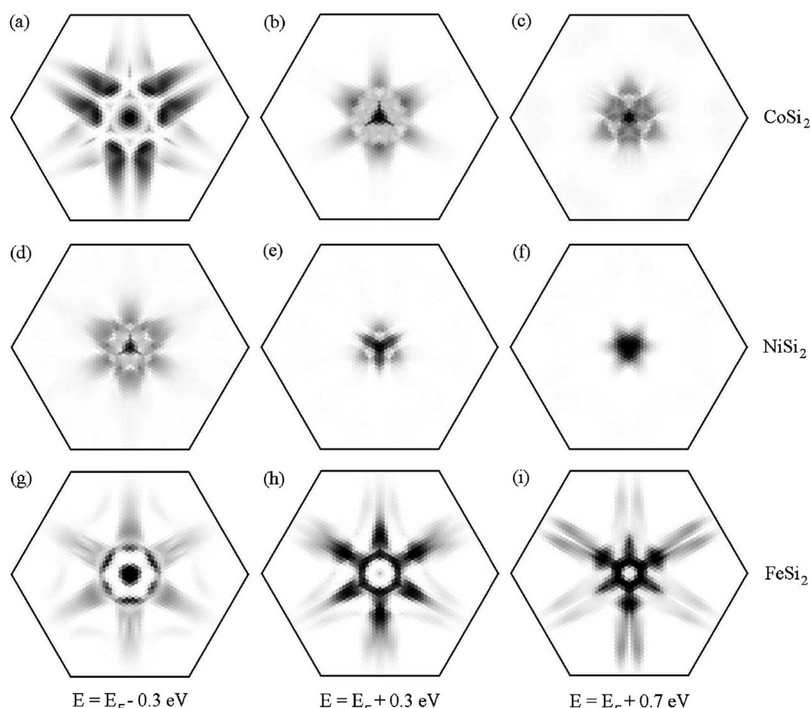

FIG. 2. Evolution of the current distribution in the first Brillouin zone of (111)-oriented [(a)–(c)] $CoSi_2$, [(d)–(f)] $NiSi_2$, and [(g)–(i)] γ-$FeSi_2$ surfaces as a function of the charges' energy. Each dot corresponds to a $\mathbf{k}_{\parallel}$ vector, and a gray scale is used to represent the density of current associated with each vector.

IV. TRANSMISSION AT THE METAL DISILICIDE/SILICON INTERFACE

The problem of the charge transmission at the metal/semiconductor interface is twofold. As already mentioned in the Introduction, the first limitation for the electrons to cross the interface is known as quantum reflection. These back-scattering effects occur because the symmetry-induced selection rules (i.e., the reciprocal space current distribution) restrict the possibilities to simultaneously conserve energy and momentum. Thus, any particle of energy E and momentum $\mathbf{k}_{\parallel}$ will be allowed to cross the interface with unit probability only if an electronic state with the same E and $\mathbf{k}_{\parallel}$ is available in the semiconductor side. This was already anticipated as a major drawback for engineering performant metal-based bipolar transistor devices.[9,29–31]

To treat this first condition on transmission, the available electronic states in the silicon channel have to be determined. To do so, the silicon channel is described using the effective mass approximation. Within this approximation, the electronic states near the conduction band minima can be described through a parabolic dispersion relation as

$$E(\mathbf{k}) = \frac{\hbar^2\mathbf{k}}{2m^*}, \tag{8}$$

where m^* is the effective mass for silicon. In the three-dimensional BZ, the dispersion relation gives rise to six ellipsoids that have to be projected on the two-dimensional BZ of the interface. In the case of the (111)- and (100)-oriented silicon substrates, the ellipsoids project as ellipses presented in Fig. 3. The position of the center of the projected ellipses depends on the chosen surface. We have used the usual effective masses in the longitudinal ($m_l^*=0.92$) and transverse ($m_t^*=0.19$) directions. Hence, for the (111) surface, the conduction band minima are projected as ellipses near the six equivalent M points of the Brillouin zone (Fig. 3, left). In contrast, the projection of the conduction band minima onto the (100) silicon surface gives four ellipses near the four equivalent M points and one circle centered at the Γ point (Fig. 3, right). When increasing the energy above the conduction band minimum (CBM), the ellipses broaden as depicted in Fig. 3 for $E=0.1$ eV and $E=0.4$ eV above CBM. Rigorously, the small part of the ellipsoids that is projected outside the first BZ should be brought back by a translation of a reciprocal lattice vector. However, the effect of this folding is expected to be small for our problem, and it will be neglected. The effective mass approximation remains valid only for a small range of energies above CBM. In the device simulations, voltage conditions will then be kept so that the energy of the injected electrons should be less than 1 eV above CBM.

In order to take into account quantum reflection phenomena for the transmission at the interface, the metal electronic states that, for a given energy, match available states with the same $\mathbf{k}_{\parallel}$ in the silicon channel have to be determined. Con-

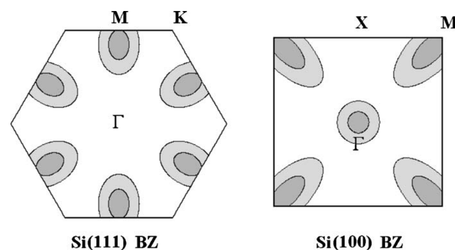

FIG. 3. First Brillouin zone for Si(111) (left) and Si(100) (right) surfaces with conduction band minima as projected ellipses within the effective mass approximation. Light and dark gray ellipses correspond to energies of 0.4 and 0.1 eV above the conduction band minimum, respectively.

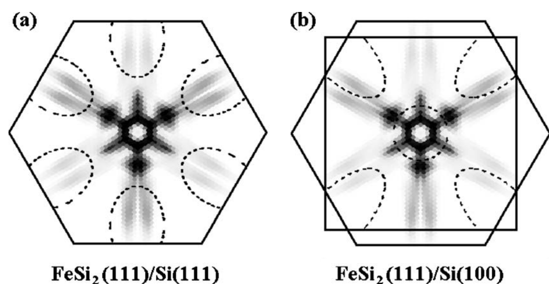

FIG. 4. Superimposition of the disilicide Brillouin zone with (a) the (111)-oriented and (b) the (100)-oriented silicon substrate, with the corresponding projected conduction band minima for E=CBM +0.5 eV. The energy and momentum conservation laws for the electron transmission are treated using a "graphical" method, i.e., by only keeping, at a given energy, the current contributions that superimpose on the inside of the silicon ellipses.

sequently, only the current contributions the momentum of which is inside the projected ellipses of the semiconductor will be kept. Figure 4 presents the superimposition of the current distribution in the metal BZ of the (111) interface on the projected conduction band minima in the (111)- [Fig. 4(a)] and the (100)- [Fig. 4(b)] oriented silicon substrate. Depending on the orientation of the silicon channel, the transmission will be different since the matching of $\mathbf{k}_{\parallel}$ vectors is not the same due to differently projected ellipses in the silicon's BZ. In particular, Fig. 4 clearly shows that, in the case of the (100)-oriented silicon substrate, the projection of CBM around the Γ point would substantially increase the transmission of electrons since a large part of the current distribution for all the three metal disilicides is focused at the center of their respective BZ. The performances of disilicide-based SB-MOSFETs should then also be strongly dependent on the silicon channel orientation. The simulation of the devices' characteristics in Sec. VI will allow one to comment and develop on that particular point.

The second condition on electron transmission results from quantum mechanics selection rules that yield to an additional backscattering probability at the interface. Indeed, there is a quantum probability that a charge that satisfies the energy and momentum conservation when crossing the disilicide/silicon interface would still be reflected. Several models exist to take into account this reflection probability. In principle, this problem should be treated within a two-dimensional, but complex, model based on Jones zone[32] methodology. It has been shown though[20] that a simpler one-dimensional model gives very similar results for the energy range we are interested in. This one-dimensional (1D) methodology will then be used to calculate the electron backscattering probability.

In a 1D model (Fig. 5), the probability for an electron arriving at the interface with a momentum k_M to be transmitted with a momentum k_{SC} is straightforwardly given as

$$T_{1D}(E) = \frac{4k_M k_{SC}}{(k_M + k_{SC})^2}. \tag{9}$$

Since the symmetry-induced rules (i.e., energy and momentum conservation) have been treated in a two-dimensional

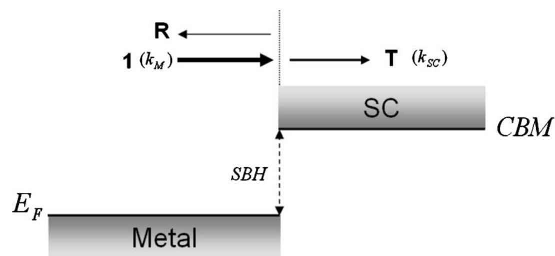

FIG. 5. Schematic representation of the 1D interface model. The incident (1) electron reaches the interface with momentum k_M. Part of the electronic wave is transmitted (T) to the semiconductor with momentum k_{SC}, whereas another part is backscattered (R) to the metal.

model, it is necessary to establish a mapping with this 1D model. The one-dimensional wave vectors k_M and k_{SC} are then expressed from the corresponding two-dimensional ones from the relations

$$k_M(E_1) = \sqrt{\frac{2E_1}{\hbar^2} - k_{\parallel}^2}, \tag{10}$$

$$k_{SC}(E_2) = \sqrt{\frac{2m_{\perp}^*(E_2 - CBM)}{\hbar^2}}, \tag{11}$$

where E_1 is the energy measured from the bottom of the metal band and $k_{\parallel}^2 = k_x^2 + k_y^2$, with k_x and k_y the components of the incoming states' wave vector. $m_{\perp}^*$ is the effective mass for silicon in the direction perpendicular to the interface [$m_{\perp}^*=0.258$ for Si(111), $m_{\perp}^*=0.19$ for Si(100)] and E_2 the energy measured with respect to CBM, the energy of the conduction band minimum of the semiconductor.

In some cases, the final current measured out of the silicon channel can be sensitive to back injection of current from the semiconductor to the metal, resulting from different scattering processes in the channel that are neglected in the present work. However, it would be possible to take into account this back-injection effect by multiplying the 1D transmission coefficient of Eq. (7) by a factor $S(E)$ that reduces, in an effective way, the transmission probability (see, for instance, Ref. 33).

Considering these two conditions, a total quantum mechanical transmission coefficient can be defined. This transmission coefficient (which is dimensionless) takes into account both the symmetry-induced conservation laws and the quantum probability of reflection when the first condition is satisfied. It corresponds to the density of current that crosses the interface divided by the total density of current that reaches the interface in the metal side.

In a SB-MOSFET configuration, this transmission coefficient will strongly depend on the voltage conditions applied to the transistor. These are of two kinds: V_{ds} is the bias voltage applied between the source and drain electrodes, and V_g is the gate voltage. The effect of these voltages on the band diagram of the device is very different. At equilibrium (V_{ds} $=V_g=0$ V), the position of the bottom of the semiconductor conduction band differs from that of the metal Fermi level by

TABLE I. Schottky-barrier heights for $NiSi_2$, $CoSi_2$, and γ-$FeSi_2$ taken from the literature.

Disilicide	SBH (eV)	Reference
$NiSi_2$	0.66	13, 34
$CoSi_2$	0.64	13, 35
γ-$FeSi_2$	0.68	13

a value equal to the SBH. A bias voltage applied between the source and drain electrodes will shift in energy the chemical potential of the two electrodes, thus modifying the shape of the energy barrier at the metal/semiconductor interfaces. This modification will be introduced in the compact model as described hereafter. The effect of the gate voltage is more important in the light of the calculation of a transmission coefficient as described in this section. Indeed, a bias voltage V_g applied on the MOSFET gate will shift the position of the conduction and valence bands of the semiconductor by a value of $-eV_g$. Hence, the available electronic states in the semiconductor side for the energy and momentum conservation selection rule will change with the gate bias. Thus, the transmission coefficient has to be computed for every desired applied gate voltage. Since this transmission coefficient will be used as an input for the compact model simulations of SB-MOSFET current-voltage characteristics, it has been calculated for a large enough gate voltage window ($-0.4 < V_g < +1.0$ V, with a step of 0.05 V) to allow accurate and reliable device simulations. The energetic diagram of the junction at equilibrium has been established with respect to the SBH values gathered in Table I.

An example of the evolution of the transmission coefficient with respect to the energy for the case of $V_g = +1.0$ V is presented in Fig. 6. We have considered the case of (111)-oriented metal disilicide in contact with both the (111) silicon surface (upper panel of Fig. 6) and (100) one (lower panel of Fig. 6). The results show that the transmission depends not only on the chosen orientation but also on the nature of the metal disilicide as the current distributions previously suggested. Consequently, the transmission is much lower in the case of (111)-oriented silicon substrate ($T_{max} \approx 0.18$) than in the case of the (100) orientation ($T_{max} \approx 0.45$). This result can be easily understood by the fact that most of the charge distribution at the interface is located around the center of the BZ, where no electronic states in the semiconductor side are available for momentum conservation in the case of (111) orientation. In contrast, the conduction band minima partly project as a circle around the Γ point in the case of (100)-oriented silicon, thus improving the transmission. Additionally, Fig. 6 also shows that the shape and intensity of the transmission curves differ from one disilicide to another. This is particularly striking in the case of the (111)-oriented silicon, for which the transmission is much more important for γ-$FeSi_2$ than for $NiSi_2$ and $CoSi_2$, especially at high energies (upper panel of Fig. 6). For the (100)-oriented semiconductor, the best case is obtained for $NiSi_2$, for which the transmission is high even at low energies, in striking contrast with the case of (111)-oriented silicon.

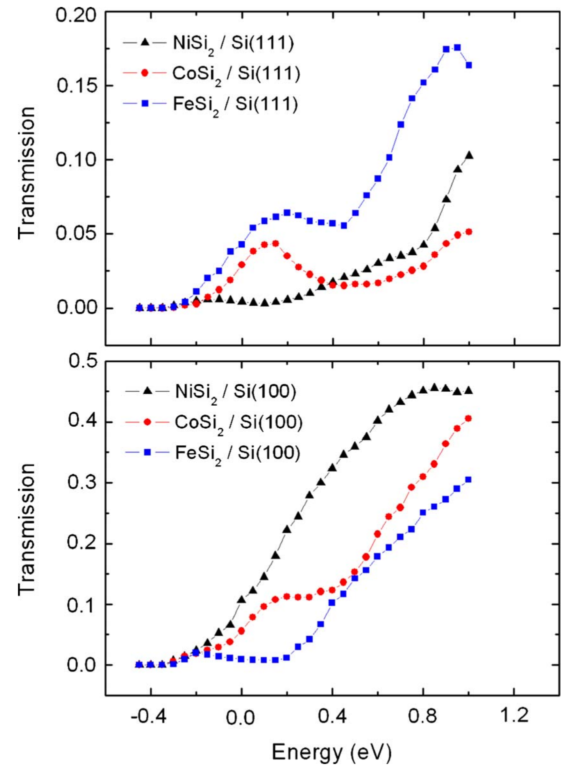

FIG. 6. (Color online) Evolution of the transmission coefficient as a function of energy for a gate voltage of 1 V for $NiSi_2$ (black ▲), $CoSi_2$ (red ●), and γ-$FeSi_2$ (blue ■). The curves in the upper panel correspond to (111)-oriented disilicides in contact with the (111)-oriented silicon substrate, whereas curves in the lower panel correspond to (111)-oriented materials in contact with (100)-oriented silicon.

The nature of the electronic propagation within the metal (due to the electronic structure of the disilicide) has already been demonstrated to have a strong influence on the charge transmission at the interface. The materials' nature and orientations, through the energy and momentum conservation laws, should then give substantially different behaviors as far as the device current-voltage characteristics are concerned. In the following section, the simulation of such curves, by means of a compact model, will confirm this prediction. The device simulations, by incorporating the atomistic transmission coefficient, will then give insights into the optimization of SB-MOSFETs in the light of preferential disilicide nature and silicon orientation.

V. COMPACT MODEL FOR THE SCHOTTKY-BARRIER METAL OXIDE SEMICONDUCTOR FIELD-EFFECT TRANSISTOR

The theory of the compact model starts with a consideration of a simplified band diagram along the channel direction. It is composed of two injecting regions close to the contacts and a midlength region (Fig. 7). In the long-channel case, this latter region is flat, its energetic level being essentially determined by the Si-NW capacitance, which is assumed to dominate over the insulator capacitance.[36,37] For a

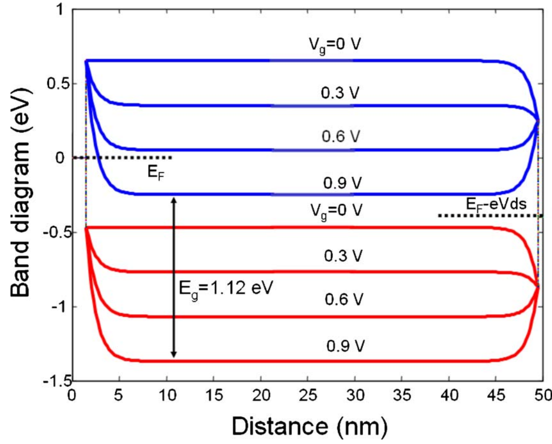

FIG. 7. (Color online) Spatial band diagram deformation versus gate voltage along the channel direction, showing the bottom of the conduction band (blue/dark gray) and the top of the valence band (red/light gray).

small thickness channel forming a quasi-one-dimensional nanowire, we can further assume that the associated density of states is low enough to yield a very small silicon capacitance and associated charge. This situation is commonly referred to as the quantum capacitance limit, and we can assume that (i) the energetic level of the midlength region rigidly shifts with V_g, and that (ii) close to the contacts, the spatial band diagram can be estimated by solving the 1D Laplace equation along the transport direction.[38] For the cylindrical surrounding gate geometry considered here, the bottom of the conduction band profile at the source region close to the disilicide reservoirs can be written as

$$\mathrm{CBM}(z) = \mathrm{SBH} - eV_g\left[1 - \exp\left(-\frac{z}{z_0}\right)\right], \tag{12}$$

where $z_0 = t_{ox}/2$ is a length scale characterizing the Schottky-barrier width, and t_{ox} is the gate silicon oxide thickness. The conduction band profile close to the drain electrode is given by Eq. (12) if z is replaced by $(L-z)$ and SBH by SBH $-V_{ds}$, where L is the length of the channel. The valence band has the same profile as the conduction band, but downshifted by a value equal to the nanowire's energy gap E_g. Assuming that the channel length is small relative to the mean free path, Landauer's approach can be used to calculate the current along the structure

$$I = \frac{2e}{h}\sum_n \int_{-\infty}^{\infty} \mathrm{sgn}(E)T_n(E)[f(\mathrm{sgn}(E)(E-E_F)) - f(\mathrm{sgn}(E)(E-E_F-eV_{ds}))]dE, \tag{13}$$

where h is Planck's constant, $f(E)$ the Fermi-Dirac distribution function, and T_n the transmission probability of the nth subband. The sign function (sgn) is introduced to express both electron and hole currents in a compact manner. As is well known, within this formalism, the transmission probability plays a central role. In order to compute the total current, the current of each subband is split into two components, namely, the thermionic and tunneling currents, and then added as indicated by Eq. (13). In the case of the thermionic current, we assume $T_n(E)$ is given by Eq. (9). For the tunneling component, the transmission through a single Schottky barrier is computed using the Wentzel-Kramers-Brillouin approximation corrected by $T_{1D}(E)$ [Eq. (9)] resulting from the $\mathbf{k}_{\parallel}$-matching condition

$$T_n(E) = \exp\left[-2\int_{z_i}^{z_f} k_{SC}(z)dz\right]T_{1D}(E), \tag{14}$$

where z_i and z_f are the classical turning points. The parallel momentum $k_{SC}(z)$ is linked to the energy through the $E(k)$ dispersion relationship of the silicon, and can be expressed (for electrons) as

$$k_{SC}(z) = \sqrt{\frac{2m_{\perp}^{*}[E - \mathrm{CBM}(z) - \Delta E_n]}{\hbar^2}}, \tag{15}$$

where ΔE_n refers to the bottom of the nth subband relative to the bottom of the conduction band.[39] Equation (14) must be numerically solved for each energy. Since the SB-MOSFET is an ambipolar device, in general, there are four possible current contributions: electron and hole thermionic currents and electron and hole tunneling currents. In addition, depending on the magnitude of the applied bias, multiple reflections can arise between the series combination of both Schottky barriers, in the same way as it occurs in a Fabry-Pérot cavity.[40] If the bias point satisfies $V_g > V_{ds}$, a double tunneling barrier for electrons is formed. In this case, neglecting phase coherence, the transmission coefficient is given by the following expression:[41]

$$T_n(E) = \frac{T_{Sn}T_{Dn}}{T_{Sn} + T_{Dn} - T_{Sn}T_{Dn}}, \tag{16}$$

where $T_{Sn}(E)$ and $T_{Dn}(E)$ are the transmission coefficients for the source and drain barriers associated with the nth subband, respectively. It is worth pointing out that neglecting the phase coherence does not appreciably affect the I-V characteristics in the typical range of temperatures where transistors operate. Even though the spectrum of the transmission is averaged when phase coherence is disregarded, leading to a smoothed current density spectrum, the same current is obtained if the tail of the Fermi-Dirac distribution is large enough. Only at low temperature conditions, out of the range of the conventional operational window, phase coherence would need to be incorporated in the model.

VI. RESULTS OF ELECTRICAL CHARACTERISTICS FOR SCHOTTKY-BARRIER METAL OXIDE SEMICONDUCTOR FIELD-EFFECT TRANSISTORS

In this section, we discuss the consequences of the physical effects introduced and analyzed in Secs. II–IV on the electrical characteristics of SB-MOSFETs with disilicide source/drain contacts. To study the impact of taking into account the material dependence on the charge injection at the interface, we consider a long-channel cylindrical surrounding-gate SB-MOSFET, schematically presented in Fig. 8, formed with a silicon nanowire of 20 nm diameter

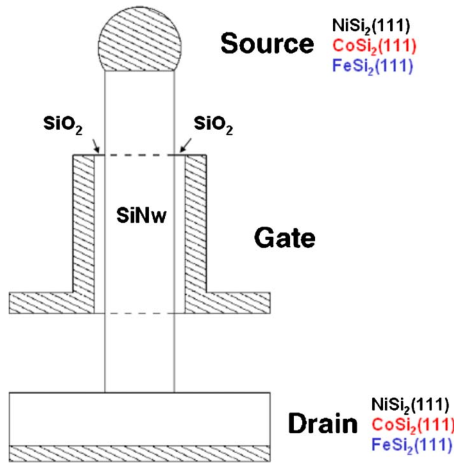

FIG. 8. (Color online) Cross section of a cylindrical surrounding-gate SB-MOSFET.

and a gate silicon oxide of 2 nm. The silicon nanowire is contacted to source and drain reservoirs made of $NiSi_2$, $CoSi_2$, and γ-$FeSi_2$, with Schottky-barrier heights given by Table I.

The transfer characteristics of the SB-MOSFET at room temperature are presented in Fig. 9 for different combinations of disilicide/Si-NW orientations using the proposed multiscale approach. We also show in the same plot the transfer characteristics obtained by switching the $\mathbf{k}_{\parallel}$ matching condition off, i.e., considering ideal injectors with transmission coefficient equal to 1 above the Schottky barrier and zero otherwise. In this study, we are concerned with the n-type region of transfer characteristics, i.e., the right branch of the transfer characteristics with respect to the ambipolar conduction point, where the dominant conduction mechanism is electron tunneling. For now, the determination of current distribution in the reciprocal space at the interface is limited, by our developed code, to the study of electron propagation. However, similar studies could be done, in principle, for the p-type region, considering, instead, the propagation and $\mathbf{k}_{\parallel}$-matching condition for holes and their transmission through the source/drain Schottky barriers with the valence band, the heights of which are $E_g-\text{SBH}$ and $E_g-\text{SBH}+eV_{ds}$, respectively.

For a proper comparison between different combinations of disilicide/Si-NW orientations, we have fixed the same off-state current (1 pA) for all the cases. This could be made in practice by tailoring the work function of the gate electrode. From Fig. 9, we can observe that the $\mathbf{k}_{\parallel}$ mismatch at the metal/semiconductor interface significantly degrades the on/off current ratio, an important figure of merit for digital applications. Specifically, more than 1 order of magnitude can be lost when this effect is taken into account. Further insights can be obtained by plotting the tunnel current spectrum (Fig. 10). From this figure, the relevant energies contributing to the current are close to the Fermi energy. Efficient contact injection should maximize transmission close to this energetic level. With regard to this issue, note that optimum on-state current can be obtained using a $NiSi_2(111)/Si(100)$ configuration, the reason being that the current distribution at the interface is just focused at the center of the two-dimensional (2D) BZ, where electronic states at the Si-NW side are available in the neighborhood of the Γ point. Qualitatively, this can be appreciated by superimposing Fig. 2(d) with the right panel of Fig. 3. A similar behavior is found for $CoSi_2(111)/Si(100)$, with a small drop in the transmission

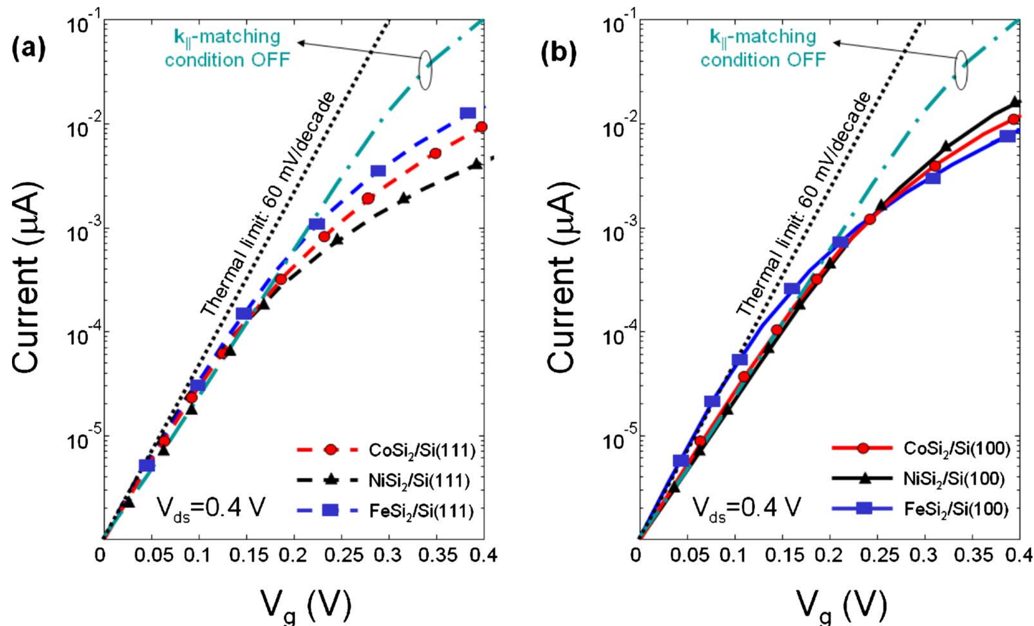

FIG. 9. (Color online) Transfer characteristics of the SB-MOSFET considering several disilicides and nanowire orientations: (111)-oriented disilicide in contact with (a) (111)-oriented or (b) (100)-oriented Si-NW. For comparison purposes, the transfer characteristics considering ideal injection from the contacts have also been represented, switching the $\mathbf{k}_{\parallel}$-matching condition off. The subthreshold slope of the SB-MOSFET is compared with the thermal limit of 60 mV/decade.

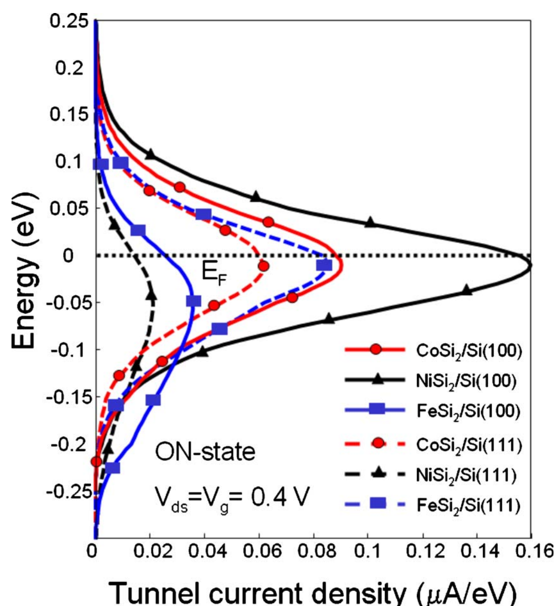

FIG. 10. (Color online) Tunnel current density of the SB-MOSFET in the on state.

coefficient (Fig. 6, lower panel) due to a more distributed pattern over the 2D BZ [Fig. 2(a)]. On the other hand, $FeSi_2(111)/Si(100)$ exhibits a very different current distribution pattern appearing as a star made of six-peaks which do not overlap too much with the projected ellipses centered at the four equivalent *M* points of the 2D BZ. A further drop of the transmission coefficient can be observed (Fig. 6, lower panel), resulting in a smaller on/off current ratio [Fig. 9(b)].

When examining, instead, disilicide heterostructures with (111)-oriented Si-NWs, a very different behavior can be observed. Note now that the CBM of the Si-NW projects into ellipses located at the six equivalent *M* points of the 2D BZ (Fig. 3, left). This effect points to a poor transmission for $NiSi_2(111)/Si(111)$ heterostructures because the current distribution pattern is focused at the center of the 2D BZ [Fig. 2(d)], where available states do not exist at the Si-NW side, giving the poorest on/off current ratio of all the analyzed combinations [Fig. 9(a)]. At the other extreme, $FeSi_2(111)/Si(111)$ provides higher on/off current ratio, because the six-peak star current distribution pattern [Fig. 2(g)] matches with available states at the (111)-oriented Si-NW. An intermediate on/off current ratio is obtained with $CoSi_2(111)/Si(111)$ heterostructures, because the central region of the current distribution pattern [Fig. 2(a)] is wasted due to the absence of available states at the Si-NW. Finally, note that the inclusion of the **k**-mismatching model does not appear to degrade the subthreshold slope and seems insensitive to the considered metal disilicide and Si-NW orientations, which are about 70 mV/decade for all the analyzed cases, even for the one using ideal injectors. Also note that short-channel effects are not included in our model. The departure from the thermal limit (=60 mV/decade) is expected because the operation principle of the disilicide heterojunction Si-NW–field-effect transistor under study is based on gate-induced Schottky-barrier width modulation instead of gate-induced barrier height modulation.[42]

VII. CONCLUSION

We have developed a multiscale approach for the simulation of electrical characteristics of metal disilicide/silicon heterojunction field-effect transistor combining atomistic tight-binding methods and compact modeling. This approach allows unveiling the role of material features in heterostructure configurations and simulating their impact on transistor performances. Specifically, the role of $\mathbf{k}_{\parallel}$ matching and quantum reflections at the metal/semiconductor interface has been extensively studied for different combinations of disilicide/silicon nanowire orientations. These effects have direct consequences on the devices' performances as the reduction of the on/off current ratio. We have shown that $NiSi_2(111)$ contacts in combination with Si(100) nanowire or $FeSi_2(111)$ with Si(111) nanowire provide optimal injection efficiency, resulting in higher on/off current ratios. We have demonstrated that the differences, in terms of device performances, between the different studied configurations are mainly driven by the symmetry selection rules of contacted materials that can be easily understood from the propagation of charge carriers in the metal disilicide and the current distribution at the interface. Quantum reflection phenomena should then be incorporated in physical and compact models for an accurate description of material-dependent injection. Similar studies as those proposed here should now be done when considering alternative materials in the search of nanodevice optimization.

The presented methodology is versatile enough to tackle SB-MOSFET device performance optimization that is currently focused on the search of materials with low Schottky-barrier (SB) heights.[43] It could also be combined with first principles calculations, as performed, for instance, for the $CoSi_2(100)/Si(100)$ interface in Ref. 44 to get an estimate of the true SB height at the interface. Finally, one notices that the quantitative understanding of material-dependent transmission properties at the silicide/silicon interfaces, and the proposed methodology for a subsequent evaluation of transistor characteristics via a compact model, could be extended to metal-based bipolar transistors, of relevance in the field of high frequency devices.[9,29–31]

ACKNOWLEDGMENTS

M.D. is grateful to CEA LETI-MINATEC for partial financial support under grant ACAV. D.J. acknowledges financial support from Ministerio de Educación y Ciencia under Project No. TEC2006-13731-C02-01/MIC. S.R. acknowledges financial support from the EU (Contract No. 015783 NODE), and the French "Action Concertée Initiative" (ACI) "Transnanofils."

*Present address: MINATEC/INPG/IMEP, 3 Parvis Louis Néel, BP 257, F-38016 Grenoble Cedex 1, France.

[1] C. Wang, J. P. Snyder, and J. R. Tucker, Appl. Phys. Lett. **74**, 1174 (1999).
[2] K. Matsuzawa, K. Uchida, and A. Nishiyama, IEEE Trans. Electron Devices **47**, 103 (2000).
[3] B. Winstead and U. Ravaioli, IEEE Trans. Electron Devices **47**, 1241 (2000).
[4] L. Sun, X. Y. Liu, M. Liu, G. Du, and R. Q. Han, Semicond. Sci. Technol. **18**, 576 (2003).
[5] J. R. Tucker, C. Wang, and P. S. Carney, Appl. Phys. Lett. **65**, 618 (1994).
[6] J. P. Snyder, C. R. Helms, and Y. Nishi, Appl. Phys. Lett. **67**, 1420 (1995).
[7] J. Tersoff, Phys. Rev. Lett. **52**, 465 (1984).
[8] Y. Taur and T. H. Ning, *Fundamentals of Modern VLSI Devices* (Cambridge University Press, Cambridge, England, 1998).
[9] A. H. Reader, A. H. van Ommen, P. J. W. Weijs, R. A. M. Wolters, and D. J. Oostra, Rep. Prog. Phys. **56**, 1397 (1992).
[10] H. von Känel, Mater. Sci. Rep. **8**, 193 (1992).
[11] X. Wallart, J. P. Nys, and C. Tetelin, Phys. Rev. B **49**, 5714 (1994).
[12] H. von Kanel, K. A. Mader, E. Muller, N. Onda, and H. Sirringhaus, Phys. Rev. B **45**, 13807 (1992).
[13] E. Bucher, S. Schulz, M. C. Lux-Steiner, P. Munz, U. Gubler, and F. Greuter, Appl. Phys. A: Solids Surf. **40**, 71 (1986).
[14] M. G. Wardle, J. P. Goss, P. R. Briddon, and R. Jones, Phys. Status Solidi A **202**, 883 (2005).
[15] Y. Wu, J. Xiang, C. Yang, W. Lu, and C. M. Lieber, Nature (London) **430**, 61 (2004).
[16] W. M. Weber *et al.*, Nano Lett. **6**, 2660 (2006).
[17] T. Yamauchi, A. Kinoshita, Y. Tsuchiya, J. Koga, and K. Kato, Tech. Dig. - Int. Electron Devices Meet. 385 (2006).
[18] M. D. Stiles and D. R. Hamann, Phys. Rev. B **40**, 1349 (1989).
[19] K. Reuter, P. L. de Andres, F. J. Garcia-Vidal, D. Sestovic, F. Flores, and K. Heinz, Phys. Rev. B **58**, 14036 (1998).
[20] P. L. de Andres, F. J. Garcia-Vidal, D. Sestovic, and F. Flores, Phys. Scr., T **T66**, 277 (1996).
[21] L. V. Keldysh, Sov. Phys. JETP **20**, 1018 (1965).
[22] P. L. de Andres, F. J. Garcia-Vidal, K. Reuter, and F. Flores, Prog. Surf. Sci. **66**, 3 (2001).
[23] F. Flores, P. L. de Andres, F. J. Garcia-Vidal, R. Saiz-Pardo, L. Jurczyszun, and N. Mingo, Prog. Surf. Sci. **48**, 27 (1995).
[24] W. B. Pearson, *Handbook of Lattice Spacing and Structures of Metals and Alloys* (Pergamon, New York, 1958).
[25] N. E. Christensen, Phys. Rev. B **42**, 7148 (1990).
[26] A. Kikuchi, T. Ohshima, and Y. Shiraki, J. Appl. Phys. **64**, 4614 (1988).
[27] N. Onda, J. Henz, E. Müller, K. A. Mäder, and H. von Känel, Appl. Surf. Sci. **56-58**, 421 (1992).
[28] G. Malegori and L. Miglio, Phys. Rev. B **48**, 9223 (1993).
[29] J. C. Hensel, A. F. J. Levi, R. T. Tung, and J. M. Gibson, Appl. Phys. Lett. **47**, 151 (1985).
[30] E. Rosencher, S. Delage, Y. Campidelli, and F. A. D'Avitaya, Electron. Lett. **20**, 762 (1984).
[31] E. Rosencher, P. A. Badoz, J. C. Pfister, F. A. d'Avitaya, G. Vincent, and S. Delage, Appl. Phys. Lett. **49**, 271 (1986).
[32] F. Garcia-Moliner and F. Flores, *Introduction to the Theory of Solid Surfaces* (Cambridge University Press, Cambridge, England, 1979).
[33] K. Reuter, U. Hohenester, P. L. de Andres, F. J. Garcia-Vidal, F. Flores, K. Heinz, and P. Kocevar, Phys. Rev. B **61**, 4522 (2000).
[34] R. T. Tung, Phys. Rev. Lett. **52**, 461 (1984).
[35] N. J. Woods and S. Hall, Semicond. Sci. Technol. **11**, 1103 (1996).
[36] S. Datta, *From Atoms to Transistors* (Cambridge University Press, Cambridge, England, 2006).
[37] For an undoped Si-NW, the flatband voltage corresponds to $V_{fb} = E_g/2 - \text{SBH} \approx -0.1$ eV. The gate voltage V_g should be interpreted as a gate voltage overdrive ($V_g \equiv V_g - V_{fb}$).
[38] D. Jiménez, X. Cartoixà, E. Miranda, J. Suñé, F. A. Chaves, and S. Roche, Nanotechnology **18**, 1 (2007).
[39] D. Jiménez, J. J. Sáenz, B. Iñíguez, J. Suñé, L. F. Marsal, and J. Pallarès, J. Appl. Phys. **94**, 1061 (2003).
[40] W. Liang, M. Bockrath, D. Bozovic, J. H. Hafner, M. Tinkham, and H. Park, Nature (London) **411**, 665 (2001).
[41] S. Datta, *Electronic Transport in Mesoscopic Systems* (Cambridge University Press, Cambridge, England, 1997).
[42] D. Jiménez, J. J. Sáenz, B. Iñíguez, J. Suñé, L. F. Marsal, and J. Pallarès, IEEE Electron Device Lett. **25**, 314 (2004).
[43] E. Dubois and G. Larrieu, J. Appl. Phys. **96**, 729 (2004).
[44] R. Stadler and R. Podloucky, Phys. Rev. B **62**, 2209 (2000).